# Direct chemical synthesis of MnO2 nanowhiskers on MXene surfaces for supercapacitor applications

ACS APPLIED MATERIALS & INTERFACES



Article

# Direct chemical synthesis of MnO2 nanowhiskers on MXene surfaces for supercapacitor applications

Raghavan Baby Rakhi, Bilal Ahmed, Dalaver H. Anjum, and Husam N. Alshareef

*ACS Appl. Mater. Interfaces*, **Just Accepted Manuscript** • DOI: 10.1021/acsami.6b04481 • Publication Date (Web): 05 Jul 2016



## Just Accepted



ACS Publications

ACS Applied Materials & Interfaces is published by the American Chemical Society.
1155 Sixteenth Street N.W., Washington, DC 20036

# Direct chemical synthesis of $MnO_2$ nanowhiskers on MXene surfaces for supercapacitor applications

**Raghavan Baby Rakhi [a,b], Bilal Ahmed [a], Dalaver Anjum[a], and Husam Niman Alshareef [a,*]**

[a]Materials Science and Engineering, King Abdullah University of Science and Technology (KAUST), Thuwal 23955-6900, Saudi Arabia

[b]Chemical Sciences and Technology division, CSIR- National Institute of Interdisciplinary Sciences and Technology (CSIR-NIIST), Thiruvananthapuram, Kerala, India, 695019

*Corresponding author: husam.alshareef@kaust.edu.sa

Phone: Office: +966-(0)2-808-4477 | Cell: +966-(0)5-44700037

## ABSTRACT

Transition metal carbides (MXenes) are an emerging class of two dimensional (2D) materials with promising electrochemical energy storage performance. Herein, for the first time, by direct chemical synthesis, nanocrystalline ε-$MnO_2$ whiskers were formed on MXene nanosheet surfaces (ε-$MnO_2$/$Ti_2CTx$ and ε-$MnO_2$/$Ti_3C_2Tx$) to make nanocomposite electrodes for aqueous pseudocapacitors. The ε-$MnO_2$ nanowhiskers increase the surface area of the composite electrode and enhance the specific capacitance by nearly *three orders of magnitude* compared to pure MXene based symmetric supercapacitors. Combined with enhanced pseudocapacitance, the fabricated ε-$MnO_2$/MXene supercapacitors exhibited excellent cycling stability with ~88% of the initial specific capacitance retained after 10000 cycles which is much higher than pure ε-$MnO_2$ based supercapacitors (~74%). The proposed electrode structure capitalizes on the high specific capacitance of $MnO_2$ and the ability of MXenes to improve conductivity and cycling stability.

## KEY WORDS

MXene, ε-$MnO_2$/MXene, specific capacitance, cycle life, symmetric supercapacitor.

## INTRODUCTION

Energy storage devices are expected to play an important role in future renewable energy systems as they can compensate the intermittent nature of renewable energy sources[1-4]. Electrochemical capacitors or pseudocapacitors, with their long cycle life, high power density and fast charge/discharge properties are considered an important class of energy storage devices for high power applications[5-8]. However, the practical applications of these devices are limited, as their energy density values are much lower in comparison with batteries[9-10]. Hence, significant research activities have been devoted to the design and development of high energy density supercapacitors to cater for both high power and energy density requirements for next-generation energy storage devices[4, 11-14]. To serve this purpose, new electrode materials with improved energy density need to be developed without any compromise on cycling stability and power density. Enhancement in energy density can be achieved by the use of hybrid composite electrode materials with high specific capacitance[6, 9, 12, 15-17]. A hybrid composite electrode material can be prepared by the insertion/dispersion of a pseudocapacitive material (transition metal oxide/conducting polymer) over a carbon material[12, 18-21].

MXenes, a family of two dimensional early transition metal carbides are emerging as unique layered chemically modified carbon materials with potential for electrochemical energy storage device applications due to their superior characteristics of high in-plane electrical conductivity, large surface area, and hydrophilic surfaces with metallic conductivity[22-28]. MXenes are produced by etching out of the "A" layer from the layered MAX phases ($M_{n+1}AX_n$) [where "M" is an early transition metal, "A" is a group A (mostly Al or Si) element, "X" is carbon and/or nitrogen, and n = 1, 2, or 3]. MXenes, themselves are denoted as $M_{n+1}X_nT_x$, where T represents surface termination groups (-O, -OH, and -F) left over from the etching process and

x is the number of terminating groups[29]. The use of MXenes as intercalation electrode material for a wide range of cations such as $Li^+$, $Na^+$, $K^+$, $NH^{4+}$, $Mg^{2+}$ and $Al^{3+}$, has been demonstrated by Gogotsi *et al*.[30-32]. Electrochemical energy storage properties of MXenes can be modified either by tuning post etch annealing conditions[33] or by decorating the MXene sheets with metal ions[34]. MXene electrodes prepared by conventional methods exhibit lower gravimetric specific capacitance as compared to graphene based electrodes. This can be easily explained by comparing the BET surface area values for these materials. Average BET surface area value reported for MXenes is in the range of 7- 30 $m^2/g$ [33], whereas for graphene it is in the range of 100-500 $m^2/g$ [35-36]. So the latter presents more electrolyte accessibility and better supercapacitive performance.

The electrochemical energy storage performance of MXenes may be improved considerably upon surface decoration of MXenes with pseudocapacitive materials. Among various pseudocapacitive transition metal oxides investigated for supercapacitors, $MnO_2$ is of great interest due to its low cost, low toxicity, natural abundance, high theoretical pseudocapacitance (about 1370 F $g^{-1}$) and friendly interfacial properties with carbon materials[37-40]. So far, to the best of our knowledge, preparation and electrochemical energy storage properties of $MnO_2$/MXene hybrids has not been reported. In the present work, ε-$MnO_2$ nanowhiskers are deposited over MXene ($Ti_3C_2T_x$ and $Ti_2CT_x$) nanosheets by direct chemical synthesis to improve the specific capacitance of the latter. Among the different phases of $MnO_2$, ε phase is well known for its electrochemical activity[41-45]. The introduction of the $MnO_2$ nanowhiskers increase the electrolyte accessible surface area and also makes an additional contribution of pseudocapacitance, at the same time, the cycling stability of MXenes can improve the overall cycling performance of the composite compared to $MnO_2$ electrode.

Therefore, in this study, symmetric supercapacitors are fabricated using ε-$MnO_2$/$Ti_2CT_x$ and ε-$MnO_2$/$Ti_3C_2T_x$ composites, and their performances are compared with that of pure MXene based and pure $MnO_2$ based symmetric supercapacitors.

## EXPERIMENTAL

### Synthesis of MXenes

Two-dimensional titanium carbide nanosheets were synthesized by exfoliation of commercially available $Ti_2AlC$ (-325 mesh, MAXTHAL 211, Kanthal Sweden) powders following a similar procedure as reported by Naguib *et al.*[22]. To obtain $Ti_3AlC_2$ phase, a mixture of commercially available $Ti_2AlC$ (Maxthal 211) and TiC (Sigma Aldrich) was heated to 1350 °C for 2 h under constant flow of Ar gas. The as-prepared $Ti_3AlC_2$ powder was treated with 50% aqueous HF solution for 18 h at RT. To prepare the lightest MXene $Ti_2CTx$, The commercially avialable $Ti_2AlC$ powder was immersed in 10% Hydrofluoric Acid (HF) for 10 h at room temperature (RT). In both the cases, the resulting suspensions were washed with deionized water for several times and then filtered to get 2D titanium carbide nanosheets (MXenes). The as-prepared MXenes ($Ti_2CT_x$ and $Ti_3C_2T_x$) were then annealed at 500K, in Ar atmosphere for 2 h. The final products are denoted as $Ti_2CT_x$_Ar and $Ti_3C_2T_x$ _Ar.

### Synthesis of metal oxide directly on MXene sheets

For the preparation of ε-$MnO_2$/MXenes, 200 mg of MXenes were dispersed in 35 mL of an aqueous solution, containing 10 mM of $MnSO_4$, by ultrasonication for 5 min. To allow impregnation of the MXene by $MnSO_4$, the suspension was then maintained at a controlled temperature of 60 ºC for 30 min under magnetic stirring. A 150 mL aqueous solution containing

33 mM of $KMnO_4$, previously heated at controlled 60 ºC, was then gradually added to the agitated suspension. This mixture was maintained at 60 ºC under agitation for 15 min and then washed, filtered and vacuum dried at 80 ºC for approximately 10 h. The proportion of the components in the final composite was estimated by weighing the final product in the dried state. (MXene to $MnO_2$ ratio 1:1). The schematic of the synthesis of $MnO_2$/MXene composite is illustrated in **Fig. 1.**

**General characterization of composites**

Powder X-ray diffraction patterns of the nanocomposite materials were obtained using a Bruker D8 ADVANCE machine equipped with Cu $K_\alpha$ radiation ($\lambda$= 0.15406 nm). BET surface area of the samples was determined using surface area and porosimetry system 'Micromeritics' (ASAP 2420) at 77 K. Before measurements, the samples were dried at 70 ˚C for 10 h in a Vacuum oven and then degassed at 150 ˚C for 12 h until the vacuum was less than 2 µm Hg. The surface morphology and microstructure of the samples were investigated using scanning electron microscopy (SEM, FEI Helios NanoLab) and transmission electron microscopy (TEM, FEI Titan).

**Preparation of electrodes and electrochemical measurement**

Each one of the active materials ($Ti_2CT_x$, $Ti_3C_2T_x$, ε-$MnO_2$/$Ti_2CT_x$ or ε-$MnO_2$/$Ti_3C_2T_x$ ) was mixed with polytetrafluoroethylene (PTFE) binder and Acetylene Black- which was added to create a conductive network in-between the MXene sheets- in a mass ratio of 90:5:5 and dispersed in ethanol. The resulting mixture was homogenized by ultrasonication and coated onto the conductive carbon cloth (ELAT, Nuvant Systems Inc.) substrate (area 1.13 $cm^2$) , which was followed by drying at 80 ˚C for 12 h in a vacuum oven. Each fabricated supercapacitor electrode contained ~**4 mg** of active material (MXene or $MnO_2$/MXene) with an average thickness of ~**28**

**µm**. Two symmetric electrodes, separated by a thin polymer separator (Celgard® 2501) in 30 wt % KOH aqueous electrolyte, were sandwiched in a supercapacitor coin cell (CR2032, MTI). The electrochemical properties of the supercapacitor electrodes were measured in **symmetric two electrode** configuration by cyclic voltammetry (CV) and galvanostatic charge-discharge (CD) measurements using CHI 660D electrochemical work station. Electrochemical impedance spectroscopy (EIS) measurements of the fabricated supercapacitors were conducted using a Modulab (Solartron Analytical) electrochemical workstation. The two electrode configuration is selected as it better mimics the configuration of a real supercapacitor[46].

## RESULTS AND DISCUSSION

The presence of $MnO_2$ along with $Ti_2CT_x$_Ar and $Ti_3C_2T_x$_Ar MXenes are confirmed from the powder XRD patterns of the composite samples shown in **Fig. 2a and b** respectively. The additional broad peaks present in the XRD patterns of $MnO_2/Ti_2CT_x$_Ar (**Fig. 2a**) and $MnO_2/Ti_3C_2T_x$_Ar (**Fig. 2b**) at approximate 2θ values 22.2 º, 36.6º, 41.7º, 55.6º, and 66.1º can be readily attributed to the (001), (100), (101), (10 2), and (110) reflections from polycrystalline orthorhombic ε-$MnO_2$, according to the JCPDS X-ray-diffraction standard card, No. 00-030-0820. The broad peaks reveal a low degree of crystallinity of the ε-$MnO_2$ on MXene sheets. A small amount of anatase $TiO_2$ which was produced by the local heat generated during HF treatment of MAX phase is also present in all these samples. The nitrogen adsorption and desorption isotherms of Ar annealed HF treated MXenes ($Ti_2CT_x$_Ar and $Ti_3C_2T_x$_Ar) and their composites with ε-$MnO_2$ (ε-$MnO_2/Ti_2CT_x$_Ar and ε-$MnO_2/Ti_3C_2T_x$_Ar) are shown in **Fig. 2c.** The Brunauer–Emmett–Teller (BET) surface area values calculated for $Ti_2CT_x$_Ar, $Ti_3C_2T_x$_Ar, ε-$MnO_2$/ $Ti_2CT_x$_Ar and ε-$MnO_2/Ti_3C_2T_x$_Ar are respectively 7.3, 21.1, 125.5, and 183.8 $m^2/g$.

The parental $Ti_2AlC$ MAX phases used in the present study were having an average particle size of 10-15 μm. Hence, the MXene samples prepared from those MAX phases were also having a bigger particle size, which leads to their lower surface area than that reported in our earlier work[33]. The $Ti_3AlC_2$ MAX phase was having an average particle size of 8 μm. This led to improved surface area for $Ti_3C_2Tx$ MXenes. A tremendous increase in surface area is observed in the composite upon ε-$MnO_2$ loading. This is due to the separation of MXene flakes upon ultrasonication and also from the surface area contribution from the ε-$MnO_2$ nanowhiskers. All the samples exhibit distinct hysteresis loops in the range of 0.45–1.0 $P/P_0$, indicating the presence of a mesoporous structure. The pore size distributions of the samples calculated by desorption isotherms using Barret-Joyner-Halenda (BJH) method are shown in **Fig. 2d**. The average pore width of the MXene samples decreases upon ε-$MnO_2$ loading, indicating that the ε-$MnO_2$ occupy the gaps between MXene flakes. BJH adsorption average pore width values calculated for $Ti_2CT_x$_Ar, $Ti_3C_2T_x$_Ar, ε-$MnO_2$/ $Ti_2CT_x$_Ar, and ε-$MnO_2$/$Ti_3C_2T_x$_Ar are 38.01, 26.41, 12.79, and 9.80 nm respectively. BJH Adsorption cumulative volume of pores between 1.70 nm and 300.00 nm diameter for $Ti_2CT_x$_Ar, $Ti_3C_2T_x$_Ar, ε-$MnO_2$/ $Ti_2CT_x$_Ar and ε-$MnO_2$/$Ti_3C_2T_x$_Ar samples are 0.0280, 0.0540, 0.2650, and 0.4248 $cm^3/g$ respectively. Adsorption cumulative pore volume increases upon $MnO_2$ loading as the $MnO_2$ structure is highly porous.

SEM analysis was conducted to investigate the morphology of the samples before and after $MnO_2$ loading. SEM image of stacked multilayer sheets of $Ti_3C_2T_x$_Ar MXene is shown in **Fig. 3a.** The images clearly indicate that the HF treatment leads to delamination of MXenes by spreading apart the basal planes with a structure similar to that of exfoliated graphite. From SEM analysis it was confirmed that the lateral thickness of individual MXene sheets were much lower

for $Ti_3C_2TX$ MXenes (~ <6 nm) as compared to that of $Ti_2CT_x$ MXenes (~>50 nm).SEM image of ε-$MnO_2$/$Ti_3C_2T_x$_Ar (**Fig. 3b**) shows the deposition of ε-$MnO_2$ nanowhiskers throughout the surface of MXene sheets. Synthesis of $MnO_2$ nanowhiskers can be readily explained using the following reaction:

$$2KMnO_4 + 3MnSO_4 + 2H_2O \rightarrow 5MnO_2 + 2H_2SO_4 + K_2SO_4 \quad (1)$$

**Figures 3a and S1a** clearly indicate that the surfaces of $Ti_3C_2T_x$ and $Ti_2CT_x$ MXenes are rough - especially following treatment with HF and Ar. This result implies that the defects on the MXene sheets, possibly facilitate the growth of $MnO_2$ nanostructures directly on the surface of the sheets. Moreover, as explained in the introductory section, etching process leads to the formation of many surface termination groups (-O, -OH, and –F) on MXene sheets, to which $MnO_2$ can get easily attached. The porous open structure of ε-$MnO_2$ on MXene sheets is expected to contribute to the fast ion adsorption–desorption and reversible redox reactions and improved supercapacitor performance when used as electrode materials in aqueous supercapacitors. The microstructure of the MXene nanosheets and ε-$MnO_2$/MXene sample are analysed using TEM. Thin and transparent nature of MXene nanosheet is evident from the TEM image shown in **Fig. 3c** for $Ti_3C_2T_x$_Ar sample.TEM image of ε-$MnO_2$/$Ti_3C_2T_x$_Ar (**Fig. 3d)** shows the presence of whisker-like microstructures of nanocrystalline $MnO_2$ attached to the surface of MXenes. By virtue of their porous nature, large surface area, and short diffusion length for protons or alkali cations, ε-$MnO_2$ nanowhiskers are considered as promising electrode materials for energy storage devices[40]. SEM and TEM images of ε-$MnO_2$/ $Ti_2CT_x$_Ar samples are shown in the supporting information (**Fig. S1**). Analysis of spatial distribution of the elements Ti, C, Mn and O in the ε-$MnO_2$/ $Ti_2CT_x$_Ar nanocomposite was done for the HRTEM

image shown in **Fig. 4a**, using energy dispersive spectroscopy (EDS) elemental mapping, and the results are shown in **Fig. 4b-e**, indicating a uniform distribution of the elements throughout the composite. Selected area electron diffraction pattern corresponding to **Fig. 4a (Fig. 4f)** clearly shows the reflections from MXene and ε-$MnO_2$ planes with the results matching perfectly with that from XRD spectra. An additional reflection peak present in the SAED pattern is attributed to $TiO_2$, which was produced by the local heat developed at the time of etching of the MAX phase.

**Fig. 5a-d** respectively shows CV loops obtained for symmetric button cell supercapacitors based on $Ti_2CT_x$_Ar, ε-$MnO_2$/$Ti_2CT_x$_Ar, $Ti_3C_2T_x$_Ar, and ε-$MnO_2$/$Ti_3C_2T_x$_Ar samples at different scan rates of 5, 10, 20, 50 and 100 mV/s in a fixed potential range of 0-0.7 V. All the test cells retain nearly rectangular CV loops, up to a scan rate of 100 mV/s, which are characteristics for supercapacitors with excellent capacitance behavior and low contact resistance. Each curve in the CV loop is composed of a capacitive current. Absence of any redox peaks in the CV loop for the composite electrodes indicates that the electrodes are charged and discharged at a pseudo-constant rate over the complete voltammetric cycle. At any particular scan rate, for the same mass loading, CV curves of the symmetric capacitors show different areas indicating different levels of stored charge. At a constant scan rate of 10 mV/s, specific capacitances of 32.4, 77.5, 106.2, and 210.9 F/g respectively are obtained for symmetric supercapacitors of $Ti_2CT_x$_Ar, $Ti_3C_2T_x$_Ar, ε-$MnO_2$/ $Ti_2CT_x$_Ar, and ε-$MnO_2$/$Ti_3C_2T_x$_Ar samples.

Galvanostatic charge-discharge curves for the symmetric supercapacitors based on $Ti_2CT_x$_Ar, ε-$MnO_2$/$Ti_2CT_x$_Ar, $Ti_3C_2T_x$_Ar, and ε-$MnO_2$/$Ti_3C_2T_x$_Ar samples at different constant current densities are shown in **Fig. 6 a-d**. Charge-discharge curves of all the devices are nearly triangular, with reduced internal resistance at the beginning of the discharge curve. The

reduction in internal resistance may be attributable to the excellent contact of the active materials to the conducting carbon cloth substrate. Specific capacitances of 32.3, 79.9, 113.1, and 212.1 F/g respectively are obtained for symmetric supercapacitors of $Ti_2CT_x$_Ar, $Ti_3C_2T_x$_Ar, ε-$MnO_2$/ $Ti_2CT_x$_Ar, and ε-$MnO_2$/$Ti_3C_2T_x$_Ar samples, at a constant current density of 1A/g.

Values of capacitance are strictly connected with the nature and surface of the electrode/electrolyte interface. Spontaneous intercalation of $K^+$ cation from the aqueous KOH electrolyte solution makes a major contribution to the specific capacitance of MXene. $Ti_2CT_x$ and $Ti_3C_2T_x$ MXenes differ in features like Surface area, layer thickness, conductivity, electrochemically stable potential window, etc. Hence, they exhibit a difference in their electrochemical energy storage performance. The considerable increase in the specific capacitance value of metal oxide dispersed MXenes as compared to MXenes is due to the progressive redox reactions occurring at the surface and bulk of transition metal oxides through Faradaic charge transfer. Dispersion of crystalline ε-$MnO_2$ nanowhiskers -which can trap the electrolyte solution- over the surface of MXene nanosheets can increase the effective contact of the electrolyte and the active materials. The surface area and in-plane conductivity (resulting from carbon contribution) of Ti3C2Tx_Ar MXene is much higher than that of Ti2CTx_Ar MXene. This feature makes Arε-$MnO_2$/$Ti_3C_2T_x$_Ar a better supercapacitor electrode material in comparison with ε-$MnO_2$/$Ti_2CT_x$_Ar.

Specific capacitance values at different constant current densities are calculated from the charge-discharge curves, and the variations in specific capacitance with the increase in current density are plotted for the symmetric supercapacitors as in **Fig. 7a**. In all the cases, at lower current densities (below 5 A/g), the specific capacitance decreases with the increase in discharge

current density and after that, the specific capacitance tends to stabilize. At lower current densities, electrolyte ions are having maximum access to the available pores in the electrode material as they can penetrate into the inner structure of the electrode. But, as the current density increases, the effective utilization of the material is limited only to the outer surface of electrodes resulting in the reduction of specific capacitance values. The rate performance calculated at a very high current density of 40 A/g for the different supercapacitor devices based on $Ti_2CT_x$_Ar, $Ti_3C_2T_x$_Ar, ε-$MnO_2$/$Ti_2CT_x$_Ar, and ε-$MnO_2$/$Ti_3C_2T_x$_Ar samples are 76%, 91%, 69%, and 83%. Ragone plots (power density vs. energy density) of the different symmetric supercapacitors test cells are shown in **Fig. 7 b and c.** The electrochemical performance of the MXenes and the composites can be improved further by reduction in the particle size of the parent MAX phase and also by the elimination of $TiO_2$ particles present on the MXene sheets. Ice bath assisted HF etching can be helpful in reducing the local heating and thereby eliminating the possible formation of $TiO_2$.

At a constant power density of 20 kW/kg, the energy densities obtained for supercapacitors based on $Ti_2CT_x$_Ar, $Ti_3C_2T_x$_Ar, ε-$MnO_2$/$Ti_2CT_x$_Ar, and ε-$MnO_2$/$Ti_3C_2T_x$_Ar samples are 1.71, 4.96, 5.47, and 12.25 Wh/kg respectively. At a low power density of 0.7 kW/kg, the energy densities reach as high as 2.19, 5.43, 7.71, and 14.42 Wh/kg respectively for the test cells. Cyclic stability studies of the fabricated symmetric supercapacitors were conducted at a constant current density of 1 A/g and the results are compared with that of the symmetric supercapacitor made of pure ε-$MnO_2$ nanowhiskers with a mass loading of 4 mg of active material per electrode. The results are illustrated in **Fig. 7d.** At the end of 10000 CD cycles at a constant current density of 5 A/g, supercapacitors based on $Ti_2CT_x$_Ar, $Ti_3C_2T_x$_Ar, ε-$MnO_2$/ $Ti_2CT_x$_Ar, and ε-$MnO_2$/$Ti_3C_2T_x$_Ar samples retain respectively 93.3%, 94.8%, 88.1%, and

87.7% of their maximum capacitance. Whereas, pure ε-$MnO_2$ nanowhiskers based supercapacitor could retain only 74.5% of its maximum capacitance. The excellent cycling performance $MnO_2$/MXene composites can be attributed to the presence of MXenes in the composites. MXene nanosheets do not take part in faradaic reactions and moreover they improve the conductivity of the composite.

Nyquist plots (EIS spectra) for symmetric supercapacitors based on $Ti_2CT_x$_Ar, $Ti_3C_2T_x$_Ar, ε-$MnO_2$/ $Ti_2CT_x$_Ar, and ε-$MnO_2$/$Ti_3C_2T_x$_Ar samples are shown in **Fig. 8a.** These plots can be divided into two regions, with a semicircle arc in the high-frequency region and a straight line in the low- frequency region. The magnitude of the resistance of the bulk electrolyte solution ($R_s$), which is also known as the equivalent series resistance (ESR) is obtained from the x-intercept of the Nyquist plot (0.97 Ω, 0.88 Ω, 1.47 Ω, and 1.46 Ω respectively for $Ti_2CT_x$_Ar, $Ti_3C_2T_x$_Ar, ε-$MnO_2$/ $Ti_2CT_x$_Ar and ε-$MnO_2$/$Ti_3C_2T_x$_Ar samples based supercapacitors) in the high-frequency region. Delaminated MXene sheets obtained after the HF treatment offer low resistance to the electrolyte solution. The diameter of the semi-circle arc in the high-frequency region is a measure of the charge transfer resistance ($R_{ct}$) which is a measure of the internal resistance of the electrode. For the symmetric supercapacitors based on $Ti_2CT_x$_Ar, $Ti_3C_2T_x$_Ar, ε-$MnO_2$/$Ti_2CT_x$_Ar and ε-$MnO_2$/$Ti_3C_2T_x$_Ar samples, the $R_{ct}$ values are measured as 0.2 Ω, 0.4 Ω, 1 Ω, and 0.6 Ω respectively. $MnO_2$ loading slightly increases the internal resistance of the electrodes. The line at the low-frequency region making an angle 45° with the real axis is called Warburg line and is a result of the diffusion of electrolyte ions within porous electrodes. The length of the Warburg line is short for metal oxide dispersed MXenes, indicating fast ion diffusion in the porous composite electrode. The frequency response of specific capacitance of the symmetric supercapacitors, obtained from the EIS measurements is shown in **Fig. 8b**.

Specific capacitance increases with the decrease in frequency. At a frequency of 1 Hz, the capacitors retain nearly half of its maximum capacitance (@ 0.01 Hz). At high-frequency region above 1000 Hz the supercapacitors behave like a pure resistance. **Fig. S2a and b** respectively shows the Nyquist plot and the frequency response curve of specific capacitance for pure ε-$MnO_2$ electrode based supercapacitor. The capacitor has very high internal resistance in the high and medium-frequency region. Capacitive performance is exhibited only at extremely low-frequency region below 0.1 Hz. This is due to the poor conductivity of the sample. But when the $MnO_2$ is loaded on MXene nanosheets, the conductivity of the composite gets improved and the resultant composite exhibitssuperior electrochemical performance. MXenes in the nanocomposite can provide a highly effective conductive pathway to provide more efficient electrical transport from the active materials to the current collector as these they have got high in- plane conductivity and the Acetylene black used in the electrode preparation ensures inter planar conductivity. This leads to the reduction in the internal resistance and improvement in the capacitive performance and cycling stability of the ε-$MnO_2$/MXene composite electrode. The present study suggests that the electrochemical energy storage performance of MXene nanosheets can be significantly improved by the incorporating them with pseudocapacitive materials.

## CONCLUSIONS

We have demonstrated a simple chemical method to grow nanocrystalline ε-$MnO_2$ directly on MXene nanosheets to make $MnO_2$/Mxene composites for pseudocapacitor applications. A specific capacitance of 212 F/g is achieved for ε-$MnO_2$/$Ti_3C_2T_x$_Ar composite, which is nearly 3 times greater than that for pure $Ti_3C_2T_x$_Ar. Symmetric supercapacitors based

on ε-$MnO_2$/MXene composite electrodes exhibited better cycling stability (~88% after 10,000 CD cycles) than that of ε-$MnO_2$ pure based symmetric capacitor. These results suggest good potential for MXene-supported hybrid electrodes for energy storage applications.

## ACKNOWLEDGEMENTS

Research reported in this publication has been supported by King Abdullah University of Science & Technology (KAUST). Authors thank the 'Advanced Nanofabrication, Imaging and Characterization Laboratory 'and 'Analytical Chemistry Laboratory' at KAUST. R.B.Rakhi acknowledges the support of Ramanujan Fellowship, Department of Science and Technology (DST), Govt.of India and CSIR-NIIST Thiruvananthapuram, India.

## ASSOCIATED CONTENT

### Supporting Information

The Supporting Information is available free of charge on the ACS Publications website

Calculation of specific capacitance, enegy and power densities, SEM and TEM images of $Ti_2CT_x$_Ar and ε-$MnO_2$/$Ti_2CT_x$_Ar samples, Nyquist plot and specific capacitance variation as a function of frequency for supercapacitors based on pure ε-$MnO_2$ sample.

### Notes

The authors declare no competing financial interest.

## REFERENCES

1. Badwal, S. P. S.; Giddey, S. S.; Munnings, C.; Bhatt, A. I.; Hollenkamp, A. F. Emerging Electrochemical Energy Conversion and Storage Technologies. *Fron.chem.* **2014,** *2*, 79-79.
2. Deng, Y.; Xie, Y.; Zou, K.; Ji, X. Review on Recent Advances in Nitrogen-Doped Carbons: Preparations and Applications in Supercapacitors. *J. Mater. Chem.A* **2016,** *4*, 1144-1173.
3. Liu, F.; Xue, D. Electrochemical Energy Storage Applications of "Pristine" Graphene Produced by Non-Oxidative Routes. *Sci China Technol Sc.* **2015,** *58*, 1841-1850.
4. Sharifi, F.; Ghobadian, S.; Cavalcanti, F. R.; Hashemi, N. Paper-Based Devices for Energy Applications. *Renew. Sustainable Energy Rev.* **2015,** *52*, 1453-1472.
5. Wang, F.; Xiao, S.; Hou, Y.; Hu, C.; Liu, L.; Wu, Y. Electrode Materials for Aqueous Asymmetric Supercapacitors. *Rsc Adv.* **2013,** *3*, 13059-13084.

6. Yu, G.; Xie, X.; Pan, L.; Bao, Z.; Cui, Y. Hybrid Nanostructured Materials for High-Performance Electrochemical Capacitors. *Nano Energy* **2013,** *2*, 213-234.
7. Yu, Z.; Tetard, L.; Zhai, L.; Thomas, J. Supercapacitor Electrode Materials: Nanostructures from 0 to 3 Dimensions. *Energy Environ Sci.* **2015,** *8*, 702-730.
8. Zhu, Y.; Murali, S.; Stoller, M. D.; Ganesh, K. J.; Cai, W.; Ferreira, P. J.; Pirkle, A.; Wallace, R. M.; Cychosz, K. A.; Thommes, M.; Su, D.; Stach, E. A.; Ruoff, R. S. Carbon-Based Supercapacitors Produced by Activation of Graphene. *Science,* **2011,** *332*, 1537-1541.
9. Wang, G.; Zhang, L.; Zhang, J. A Review of Electrode Materials for Electrochemical Supercapacitors. *Chem Soc Rev.* **2012,** *41*, 797-828.
10. Simon, P.; Gogotsi, Y. Materials for Electrochemical Capacitors. *Nature Mater.* **2008,** *7*, 845-854.
11. Ramachandran, R.; Chen, S.-M.; Kumar, G. G. An Overview of Electrochemical Energy Storage Devices of Various Electrodes and Morphological Studies of Supercapacitors. *Int. J. Electrochem. Sci.* **2015,** *10*, 10355-10388.
12. Sun, Y.; Shi, G. Graphene/Polymer Composites for Energy Applications. *J. Polym. Sci. Part B: Polym. Phys.* **2013,** *51*, 231-253.
13. Yan, J.; Wang, Q.; Wei, T.; Fan, Z. Recent Advances in Design and Fabrication of Electrochemical Supercapacitors with High Energy Densities. *Adv.Energy Mater.* **2014,** *4,1300816 (Pages 1-43)*.
14. Shi, F.; Li, L.; Wang, X.-l.; Gu, C.-d.; Tu, J.-p. Metal Oxide/Hydroxide-Based Materials for Supercapacitors. *Rsc Adv.* **2014,** *4*, 41910-41921.
15. Chen, S.M.; Ramachandran, R.; Mani, V.; Saraswathi, R. Recent Advancements in Electrode Materials for the High-Performance Electrochemical Supercapacitors: A Review. *Int. J. Electrochem. Sci.* **2014,** *9*, 4072-4085.
16. Choi, H.; Yoon, H. Nanostructured Electrode Materials for Electrochemical Capacitor Applications. *Nanomaterials* **2015,** *5*, 906-936.
17. Meyyappan, M. Nanostructured Materials for Supercapacitors. J. Vac. Sci. Technol. A **2013,** *31, 050803 (Pages 1-14)*.
18. Lou, B.-S.; Veerakumar, P.; Chen, S.-M.; Veeramani, V.; Madhu, R.; Liu, S.-B. Ruthenium Nanoparticles Decorated Curl-Like Porous Carbons for High Performance Supercapacitors. *Sci. Rep.* **2016,** *6, 19949 (pages1-11)*.
19. Ma, H.; He, J.; Xiong, D.-B.; Wu, J.; Li, Q.; Dravid, V.; Zhao, Y. Nickel Cobalt Hydroxide @Reduced Graphene Oxide Hybrid Nanolayers for High Performance Asymmetric Supercapacitors with Remarkable Cycling Stability. *ACS Appl Mater Interfaces* **2016,** *8*, 1992-2000.
20. Ngoc Quang, T.; Kang, B. K.; Tiruneh, S. N.; Yoon, D. H. Design of Advanced Mno/N-Gr 3d Walls through Polymer Cross-Linking for High-Performance Supercapacitor. *Chem. Eur. J.* **2016,** *22*, 1652-1657.
21. Thangappan, R.; Kalaiselvam, S.; Elayaperumal, A.; Jayavel, R.; Arivanandhan, M.; Karthikeyan, R.; Hayakawa, Y. Graphene Decorated with Mos2 Nanosheets: A Synergetic Energy Storage Composite Electrode for Supercapacitor Applications. *Dalton Trans. (Cambridge, England : 2003)* **2016,** *45*, 2637-46.
22. Naguib, M.; Mashtalir, O.; Carle, J.; Presser, V.; Lu, J.; Hultman, L.; Gogotsi, Y.; Barsoum, M. W. Two-Dimensional Transition Metal Carbides. *Acs Nano* **2012,** *6*, 1322-1331.
23. Naguib, M.; Mochalin, V. N.; Barsoum, M. W.; Gogotsi, Y. 25th Anniversary Article: Mxenes: A New Family of Two-Dimensional Materials. *Adv. Mater.* **2014,** *26*, 992-1005.
24. Bhimanapati, G. R.; Lin, Z.; Meunier, V.; Jung, Y.; Cha, J.; Das, S.; Xiao, D.; Son, Y.; Strano, M. S.; Cooper, V. R.; Liang, L.; Louie, S. G.; Ringe, E.; Zhou, W.; Kim, S. S.; Naik, R. R.; Sumpter, B. G.; Terrones, H.; Xia, F.; Wang, Y.; Zhu, J.; Akinwande, D.; Alem, N.; Schuller, J. A.; Schaak, R. E.; Terrones, M.; Robinson, J. A. Recent Advances in Two-Dimensional Materials Beyond Graphene. *Acs Nano* **2015,** *9*, 11509-11539.

25. Naguib, M.; Come, J.; Dyatkin, B.; Presser, V.; Taberna, P.-L.; Simon, P.; Barsoum, M. W.; Gogotsi, Y. Mxene: A Promising Transition Metal Carbide Anode for Lithium-Ion Batteries. *Electrochem.Comm.* **2012,** *16*, 61-64.
26. Kim, S. J.; Naguib, M.; Zhao, M.; Zhang, C.; Jung, H.-T.; Barsoum, M. W.; Gogotsi, Y. High Mass Loading, Binder-Free Mxene Anodes for High Areal Capacity Li-Ion Batteries. *Electrochim Acta* **2015,** *163*, 246-251.
27. Xie, Y.; Dall'Agnese, Y.; Naguib, M.; Gogotsi, Y.; Barsoum, M. W.; Zhuang, H. L.; Kent, P. R. C. Prediction and Characterization of Mxene Nanosheet Anodes for Non-Lithium-Ion Batteries. *Acs Nano* **2014,** *8*, 9606-9615.
28. Xie, Y.; Naguib, M.; Mochalin, V. N.; Barsoum, M. W.; Gogotsi, Y.; Yu, X.; Nam, K.-W.; Yang, X.-Q.; Kolesnikov, A. I.; Kent, P. R. C. Role of Surface Structure on Li-Ion Energy Storage Capacity of Two-Dimensional Transition-Metal Carbides. *J. Am. Chem. Soc,* **2014,** *136*, 6385-6394.
29. Gogotsi, Y. Not Just Graphene: The Wonderful World of Carbon and Related Nanomaterials. *MRS Bull.* **2015,** *40*, 1110-1121.
30. Lukatskaya, M. R.; Mashtalir, O.; Ren, C. E.; Dall'Agnese, Y.; Rozier, P.; Taberna, P. L.; Naguib, M.; Simon, P.; Barsoum, M. W.; Gogotsi, Y. Cation Intercalation and High Volumetric Capacitance of Two-Dimensional Titanium Carbide. *Science* **2013,** *341*, 1502-1505.
31. Ling, Z.; Ren, C. E.; Zhao, M.-Q.; Yang, J.; Giammarco, J. M.; Qiu, J.; Barsoum, M. W.; Gogotsi, Y. Flexible and Conductive Mxene Films and Nanocomposites with High Capacitance. Proc Natl Acad Sci U S A **2014,** *111*, 16676-16681.
32. Lukatskaya, M. R.; Ren, C.; Mashtalir, O.; Dall'Agnese, Y.; Naguib, M.; Simon, P.; Barsoum, M.; Gogotsi, Y. Capactive Performance of 2d Tiitanium Carbide Based Mxenes Owing to Cation Intercalation. *ABSTR PAP AM CHEM S* **2014,** *247*.
33. Rakhi, R. B.; Ahmed, B.; Hedhili, M. N.; Anjum, D. H.; Alshareef, H. N. Effect of Postetch Annealing Gas Composition on the Structural and Electrochemical Properties of Ti2ctx Mxene Electrodes for Supercapacitor Applications. *Chem. Mater.* **2015,** *27*, 5314-5323.
34. Luo, J.; Tao, X.; Zhang, J.; Xia, Y.; Huang, H.; Zhang, L.; Gan, Y.; Liang, C.; Zhang, W. Se4+ Ion Decorated Highly Conductive Ti3c2 Mxene: Promising Lithium-Ion Anodes with Enhanced Volumetric Capacity and Cyclic Performance. *Acs Nano* **2016,** *10*, 2491-2499.
35. Bai, Y.; Rakhi, R. B.; Chen, W.; Alshareef, H. N. Effect of Ph-Induced Chemical Modification of Hydrothermally Reduced Graphene Oxide on Supercapacitor Performance. *J. Power Sources* **2013,** *233*, 313-319.
36. Lian, P.; Zhu, X.; Liang, S.; Li, Z.; Yang, W.; Wang, H. Large Reversible Capacity of High Quality Graphene Sheets as an Anode Material for Lithium-Ion Batteries. *Electrochim.Acta* **2010,** *55*, 3909-3914.
37.Zhao, J. C.; Wang, J.; Xu, J. L. Synthesis and Electrochemical Characterization of Mesoporous Mno2. *J. Chemistry* **2015,** 2015, 76803 (Pages 1-5).
38. Cao, J.; Li, X.; Wang, Y.; Walsh, F. C.; Ouyang, J.-H.; Jia, D.; Zhou, Y. Materials and Fabrication of Electrode Scaffolds for Deposition of Mno2 and Their True Performance in Supercapacitors. *J.Power Sources* **2015,** *293*, 657-674.
39. Wang, J.-G.; Kang, F.; Wei, B. Engineering of Mno2-Based Nanocomposites for High-Performance Supercapacitors. *PROG MATER SCI* **2015,** *74*, 51-124.
40. Wei, W.; Cui, X.; Chen, W.; Ivey, D. G. Manganese Oxide-Based Materials as Electrochemical Supercapacitor Electrodes. *Chem.Soc. Rev.***2011,** *40*, 1697-1721.
41. Roberts, A. J.; Slade, R. C. T. Controlled Synthesis of Epsilon-Mno(2) and Its Application in Hybrid Supercapacitor Devices. *J. Mater. Chem.* **2010,** *20*, 3221-3226.
42. Han, D.; Jing, X.; Xu, P.; Ding, Y.; Liu, J. Facile Synthesis of Hierarchical Hollow Epsilon-Mno2 Spheres and Their Application in Supercapacitor Electrodes. *J. Solid State Chem.***2014,** *218*, 178-183.

43. Lin, M.; Chen, B.; Wu, X.; Qian, J.; Fei, L.; Lu, W.; Chan, L. W. H.; Yuan, J. Controllable in Situ Synthesis of Epsilon Manganese Dioxide Hollow Structure/Rgo Nanocomposites for High-Performance Supercapacitors. *Nanoscale* **2016,** *8*, 1854-1860.
44. Chen, W.; Rakhi, R. B.; Alshareef, H. N. High Energy Density Supercapacitors Using Macroporous Kitchen Sponges. *J. Mater. Chem.* **2012,** *22*, 14394-14402.
45. Chen, W.; Rakhi, R. B.; Hu, L.; Xie, X.; Cui, Y.; Alshareef, H. N. High-Performance Nanostructured Supercapacitors on a Sponge. *Nano Lett.***2011,** *11*, 5165-5172.
46. Stoller, M. D.; Ruoff, R. S. Best Practice Methods for Determining an Electrode Material's Performance for Ultracapacitors. *Energy Environ Sci.* **2010,** *3*, 1294-1301.

## FIGURE CAPTIONS

1. Schematic of the synthesis of $MnO_2$/MXene composite
2. Powder X-ray diffraction patterns of (a) $Ti_2CT_x$_Ar and ε-$MnO_2$/ $Ti_2CT_x$_Ar samples and (b) $Ti_3C_2T_x$_Ar and ε-$MnO_2$/$Ti_3C_2T_x$_Ar samples, (c) BET nitrogen adsorption-desorption isotherms and (d) pore size distributions of $Ti_2CT_x$_Ar, $Ti_3C_2T_x$_Ar, ε-$MnO_2$/ $Ti_2CT_x$_Ar and ε-$MnO_2$/$Ti_3C_2T_x$_Ar samples
3. SEM images of (a) $Ti_3C_2T_x$_Ar, and (b) ε-$MnO_2$/$Ti_3C_2T_x$_Ar samples and High magnification TEM images of (c) $Ti_3C_2T_x$_Ar and (d) ε-$MnO_2$/$Ti_3C_2T_x$_Ar samples
4. (a) High Magnification TEM image of ε-$MnO_2$/ $Ti_2CT_x$_Ar. EDS elemental mapping of (b) Ti, (c) C, (d) Mn and (e) O. (f) SAED pattern corresponding to (a).
5. Cyclic voltammograms of symmetric supercapacitors based on (a) $Ti_2CT_x$_Ar, (b) ε-$MnO_2$/$Ti_2CT_x$_Ar, (c) $Ti_3C_2T_x$_Ar, and (d) ε-$MnO_2$/$Ti_3C_2T_x$_Ar samples at different scan rates.
6. Galvanostatic charge-discharge curves of symmetric supercapacitors based on (a) $Ti_2CT_x$_Ar, (b) ε-$MnO_2$/$Ti_2CT_x$_Ar, (c) $Ti_3C_2T_x$_Ar, and (d) ε-$MnO_2$/$Ti_3C_2T_x$_Ar samples at different current densities.
7. (a) Specific capacitances of MXene and metal oxide/MXene based symmetric supercapacitors at different current densities. (b, c) Ragone plots (power density vs. energy density) of MXene and metal oxide/MXene based symmetric supercapacitors. The energy and power densities were derived from the charge–discharge curves at different current densities. and (d) Cycling performance of different symmetric supercapacitors at a constant current density of 5 A/g (10000 charge- discharge cycles)
8. (a) Nyquist plots and (b) specific capacitance variation as a function of frequency, for supercapacitors based on $Ti_2CT_x$_Ar, $Ti_3C_2T_x$_Ar, ε-$MnO_2$/ $Ti_2CT_x$_Ar and ε-$MnO_2$/$Ti_3C_2T_x$_Ar samples.

## FIGURES

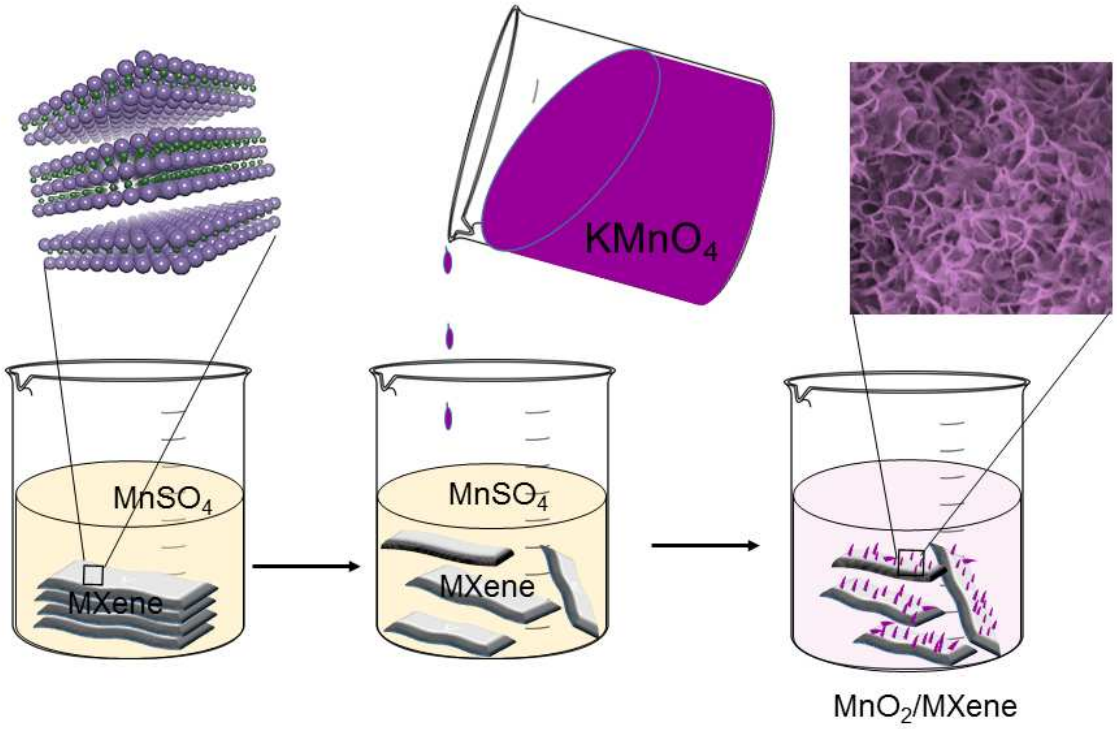


**Figure 1**

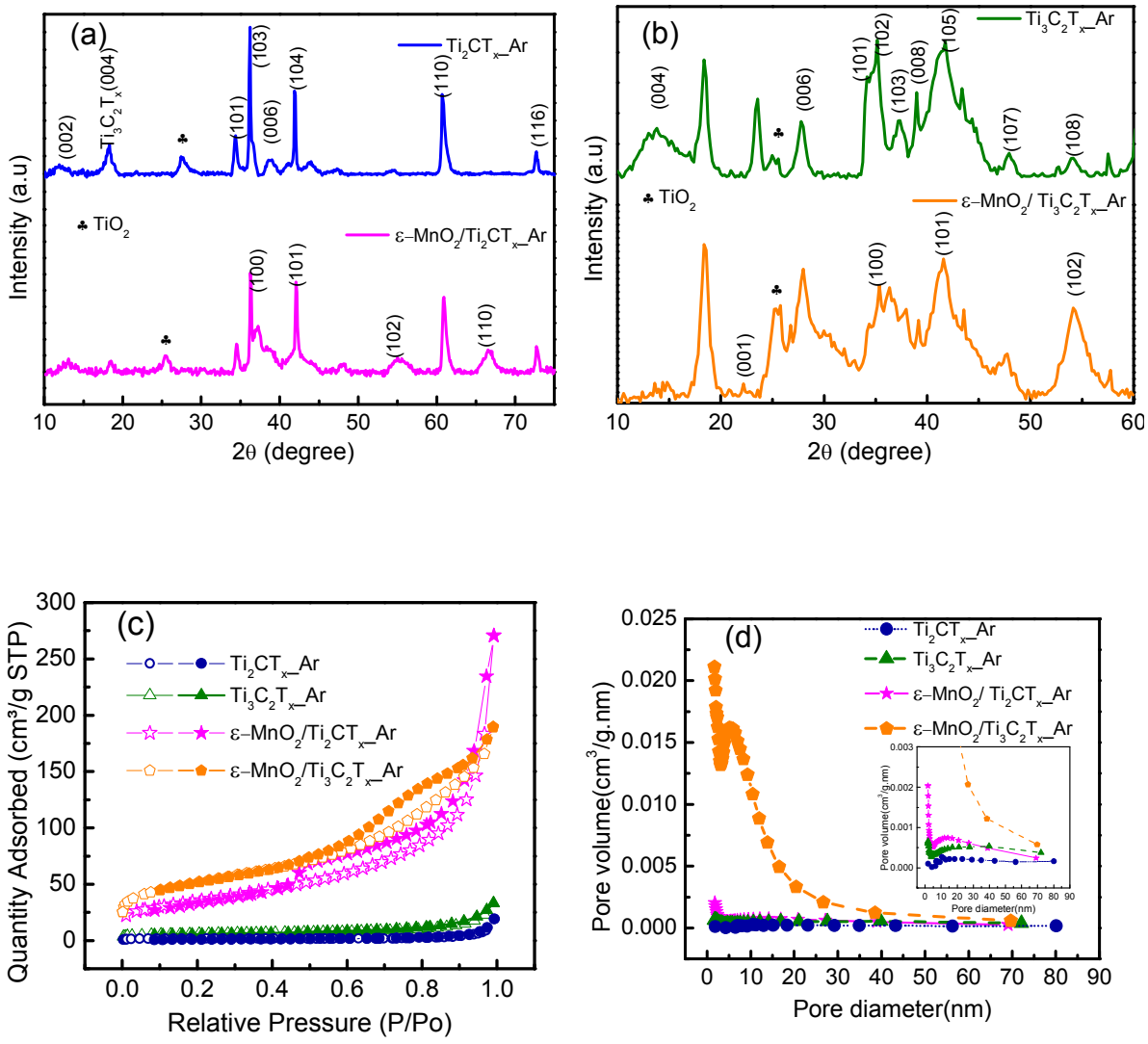
(a)
Ti2CTx_Ar
ε–MnO2/Ti2CTx_Ar
♣ TiO2
(002)
Ti3C2Tx(004)
(101)
(103)
(006)
(104)
(110)
(116)
(100)
(101)
(102)
(110)
Intensity (a.u)
2θ (degree)
(b)
Ti3C2Tx_Ar
ε–MnO2/ Ti3C2Tx_Ar
♣ TiO2
(004)
(006)
(101)
(102)
(103)
(008)
(105)
(107)
(108)
(001)
(100)
(101)
(102)
Intensity (a.u)
2θ (degree)
(c)
Ti2CTx_Ar
Ti3C2Tx_Ar
ε–MnO2/Ti2CTx_Ar
ε–MnO2/Ti3C2Tx_Ar
Quantity Adsorbed (cm³/g STP)
Relative Pressure (P/Po)
(d)
Ti2CTx_Ar
Ti3C2Tx_Ar
ε–MnO2/ Ti2CTx_Ar
ε–MnO2/Ti3C2Tx_Ar
Pore volume(cm³/g.nm)
Pore diameter(nm)

**Figure 2**

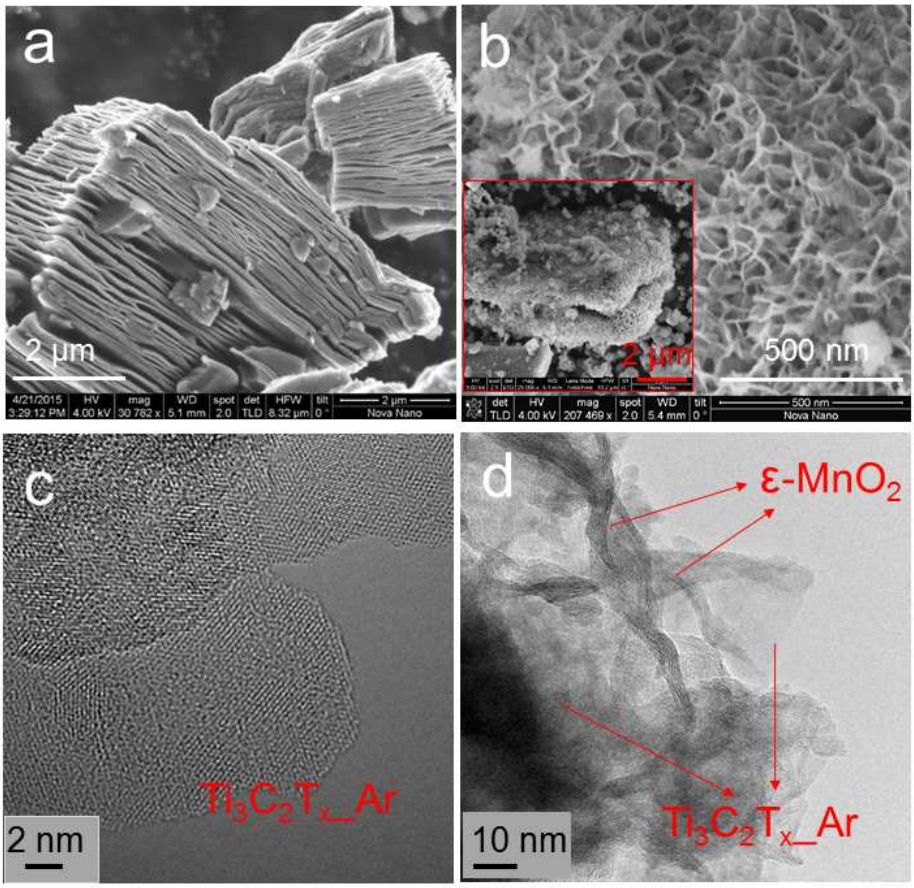


**Figure 3**

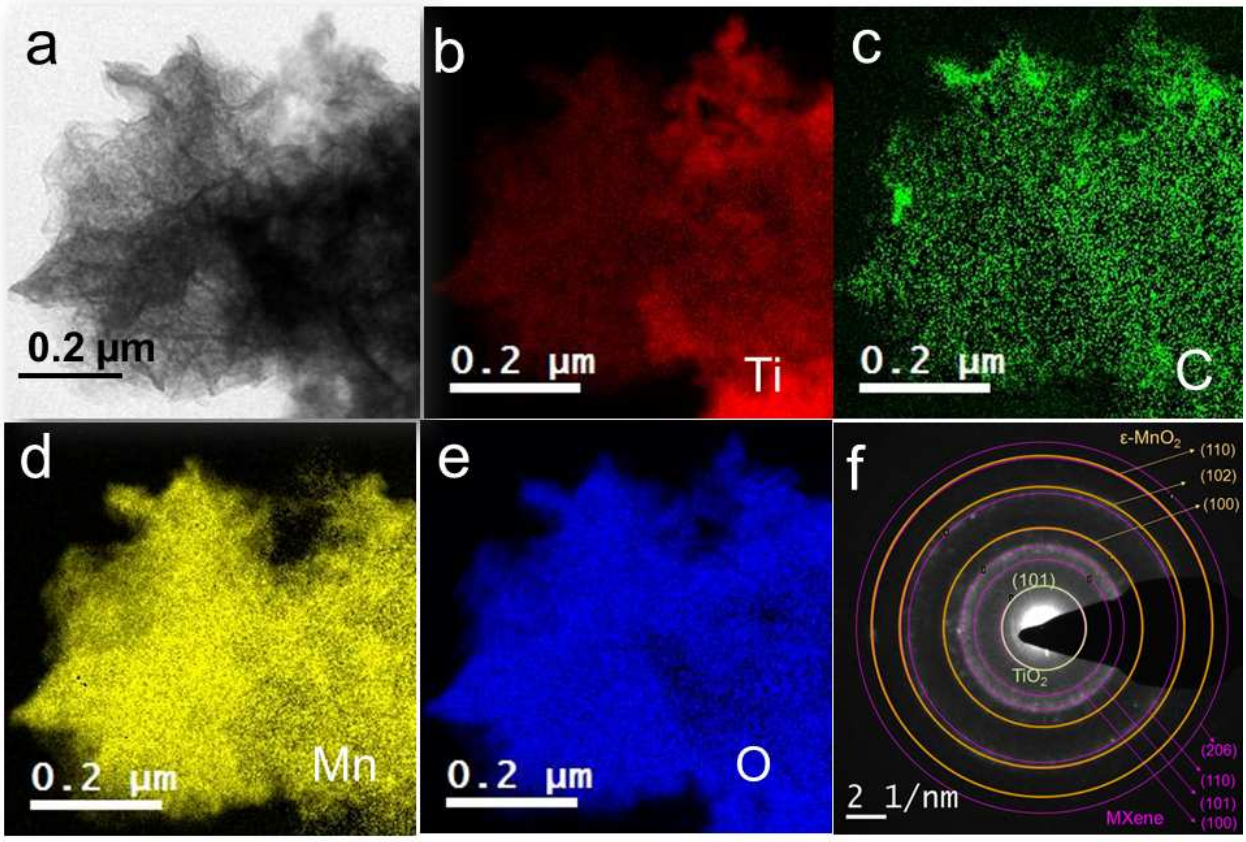
a
0.2 μm
b
0.2 μm
Ti
c
0.2 μm
C
d
0.2 μm
Mn
e
0.2 μm
O
f
ε-MnO2
(110)
(102)
(100)
(101)
TiO2
(206)
(110)
(101)
(100)
2 1/nm
MXene

**Figure 4**

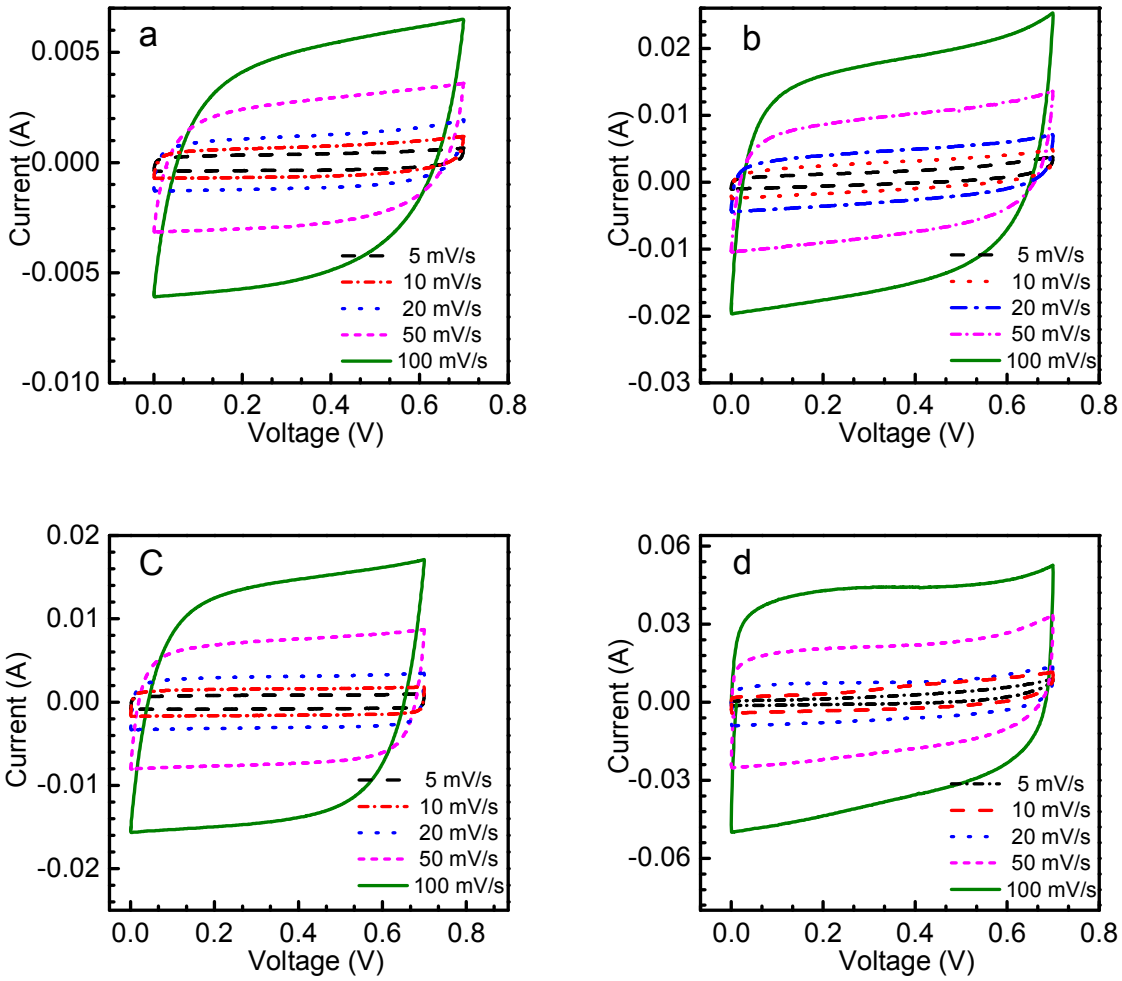


**Figure 5**

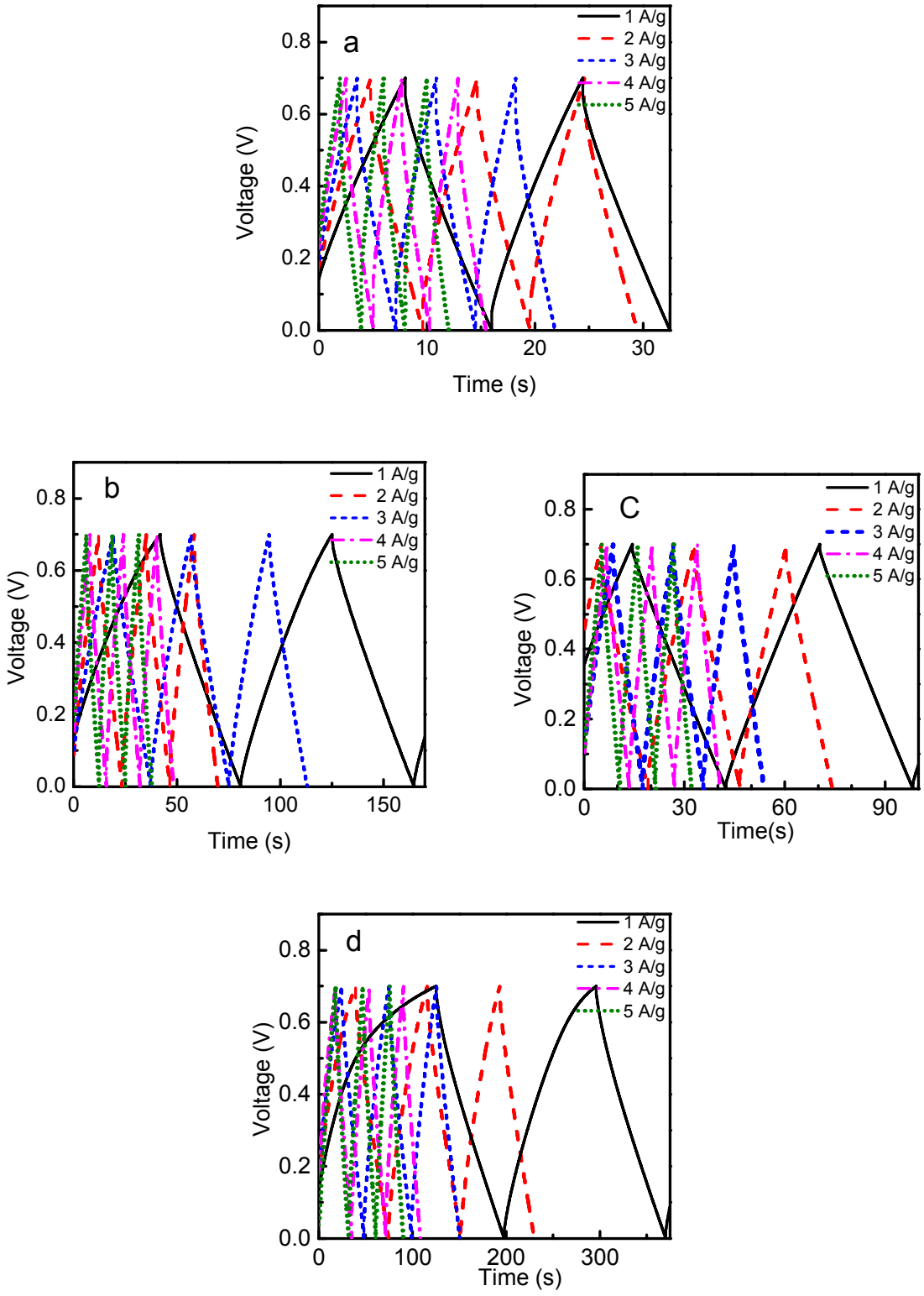


**Figure 6**

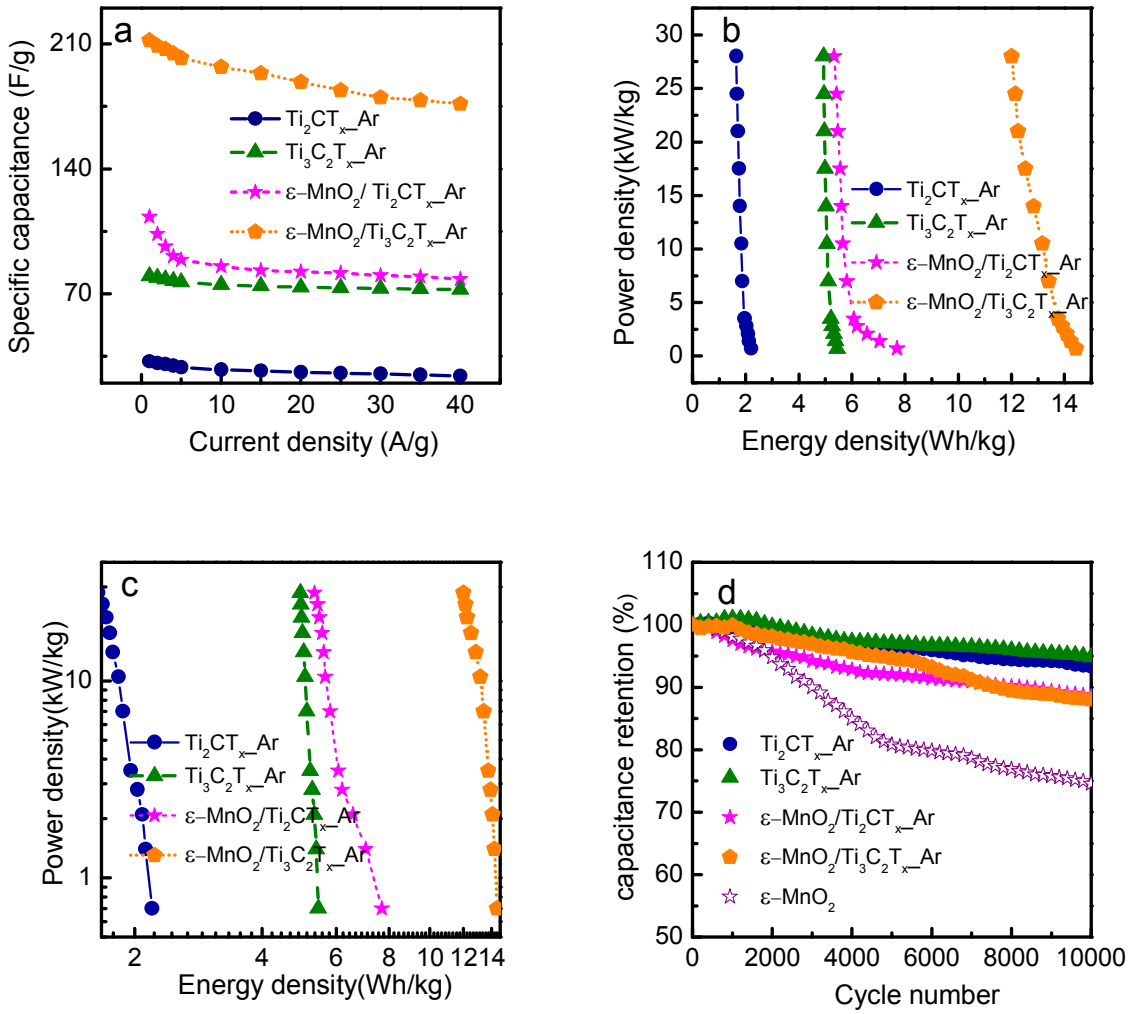
a
Specific capacitance (F/g)
Current density (A/g)
Ti2CTx_Ar
Ti3C2Tx_Ar
ε-MnO2/ Ti2CTx_Ar
ε-MnO2/Ti3C2Tx_Ar
b
Power density(kW/kg)
Energy density(Wh/kg)
c
Power density(kW/kg)
Energy density(Wh/kg)
d
capacitance retention (%)
Cycle number
ε-MnO2

**Figure 7**

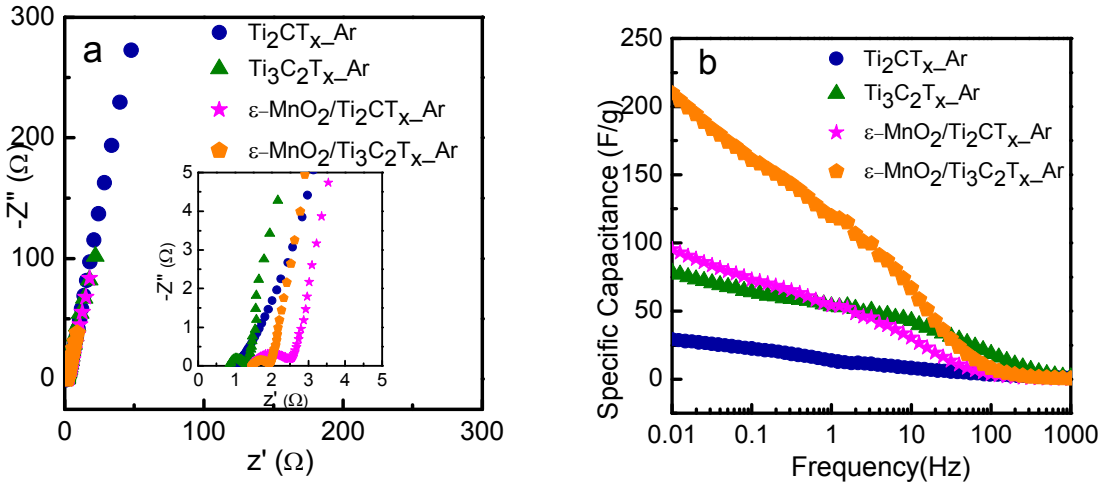
a
b
$Ti_2CT_x$_Ar
$Ti_3C_2T_x$_Ar
ε-$MnO_2$/$Ti_2CT_x$_Ar
ε-$MnO_2$/$Ti_3C_2T_x$_Ar
-Z'' (Ω)
z' (Ω)
Specific Capacitance (F/g)
Frequency(Hz)

**Figure 8**

**Table of contents image**